ACS NANO

www.acsnano.org

ARTICLE

M13-Phage-Based Star-Shaped Particles with Internal Flexibility

Arantza B. Zavala-Martínez and Eric Grelet*

Cite This: *ACS Nano* 2024, 18, 281−287

Read Online

ACCESS | Metrics & More | Article Recommendations | Supporting Information

ABSTRACT: We report on the construction and the dynamics of monodisperse star-shaped particles, mimicking, at the mesoscale, star polymers. Such multiarm star-like particles result from the self-assembly of gold nanoparticles, forming the core, with tip-linked filamentous viruses (M13 bacteriophages) acting as spines in a sea urchin-like structure. By combining fluorescence and dark-field microscopy with dynamic light scattering, we investigate the diffusion of these hybrid spiny particles. We reveal the internal dynamics of the star particles by probing their central metallic core, which exhibits a hindered motion that can be described as a Brownian particle trapped in a harmonic potential. We therefore show that the filamentous viruses and specifically their tip proteins behave as entropic springs, extending the relevance of the study of such hybrid mesoscopic analogues of star polymers to phage biotechnology.

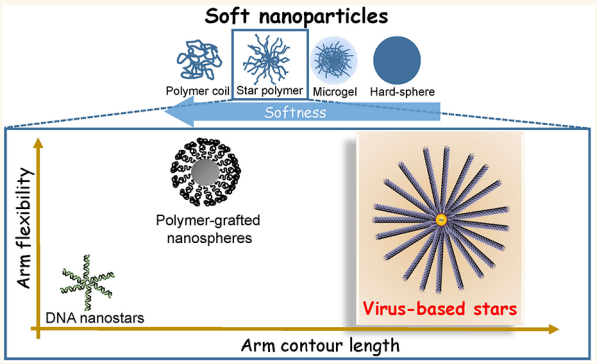

KEYWORDS: *soft particle, star polymer, single particle tracking, dynamic light scattering, diffusion, Au nanoparticle, M13 filamentous phage*

So-called "soft particles" refer to a class of objects with a dual character somewhere between hard colloids and polymer coils.[1−3] Common examples of these particles include microgels,[4−6] micelles,[7,8] and star polymers,[9−11] whose phase behaviors and dynamics change as the level of their softness increases. For hard spherical particles, which undergo transitions from a disordered fluid phase to a crystalline phase at relatively low volume fractions,[12] their Brownian diffusion can be affected by hydrodynamic or interparticle interactions.[13−15] In contrast, ultrasoft particles such as polymer coils behave as amorphous fluids even at very high volume fractions,[16] and their dynamics is controlled by the elasticity of the chains, the deformability of the core, and entanglement.[17,18] For systems in between, including microgels, made of cross-linked polymeric networks swollen by a solvent, or star polymers, consisting of long polymeric arms connected to a central core, the dynamical behavior depends also on the compressibility and interdigitation of the particles.[19−21] These interactions for soft systems can suppress crystallization and lead to direct transitions to glassy and jammed states.[4,22−24] Thus, the design of custom-made particles intermediate between the hard and ultrasoft limits plays a key-role for the general understanding of phenomena such as the origin of glass transition[25] or the formation of densely packed states.[26−28]

In this context, multiarm star-like systems, where the number, size, and flexibility of the arms are tunable, leading to variable deformability and interdigitation provide an ideal testbed for the study of the impact of "softness" on dynamics.[29,30] Polymer chains grafted on a nanosphere core represent the most simplified star-like system with tunable softness. In the limit of chains short compared to core size, the hard sphere behavior may prevail, whereas for long polymer chains, the structure and the dynamics of ultrasoft particles are expected.[31,32] For instance, star-like particles such as polymer-grafted latex or silica nanoparticles in the range of sizes from tens to hundreds of nanometers have already been achieved and used to investigate glass formation by varying the strength of interparticle interactions.[33−35] However, the main limitation of these polymer-grafted nanospheres is their high polydispersity in both size and number of arms. Moreover, the polymer chains are in the high flexibility limit, where their persistence length, L_p, is short compared to their contour length L_c,[36,37] *i.e.*, $L_p \ll L_c$.

Recently, DNA nanotechnology has provided an exquisite tool for the construction of monodisperse systems of multiarm

Received: July 5, 2023
Revised: December 7, 2023
Accepted: December 12, 2023
Published: December 19, 2023

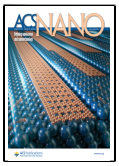

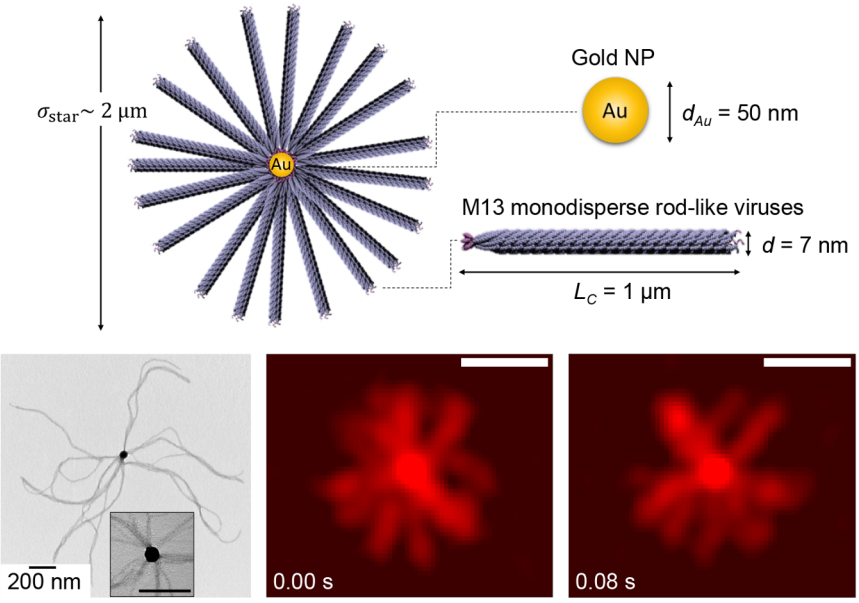

Figure 1. Hybrid M13-virus-based star particles. Top: Schematic representation of the particle structure exhibiting an urchin-like morphology and its two components: A gold nanoparticle (Au NP) as core, and arms or spines formed by tip-linked monodisperse semiflexible rod-like viruses (M13 phages). Bottom: Transmission electron microscopy image (left) and confocal fluorescence microscopy images (right) of star particles. The white scale bars represent 1 μm.

nanostar particles.[38−41] Monodisperse in size, these DNA molecular stars represent appealing systems for soft matter and nanoscience including soft particle dynamics. They differ from the polymer-grafted nanospheres in having a low number of very stiff arms, with a persistence length of $L_p \simeq 50$ nm,[42] and an arm contour length, L_c, of a few nanometers,[38,43] putting them in the $L_c \ll L_p$ limit. They are, however, difficult to study at the single particle level, because of their limited size. At higher length scale, colloids coated with ultralong DNA fragments resulting in dense spherical charged brushes, have been designed, and their phase behavior reveals fundamental properties in terms of deformation and interpenetration of the particles.[27,28]

Here, we propose a model system of monodisperse soft star-like particles composed of a gold nanoparticle core −Au NP− , linked with semirigid filamentous viruses, M13 bacteriophages, acting as spines in an urchin-like structure,[44,45] as shown in Figure 1. Thanks to their biological origin, these rod-shaped viruses are uniform in size (see Materials and Methods). They have been genetically modified to regioselectively interact via one of their tips with Au,[46] and have been already used in sensor application.[45] The self-assembly between the metallic (Au NPs) and the biological (M13 phages) components results in sparse particles, which are monodisperse in size and whose number of arms can be tuned. The persistence length of these viral arms is comparable to their contour length, *i.e.*, $L_p \sim L_c$,[47] putting them in between the polymer-grafted nanospheres and the DNA nanostars. The relative dimension of the Au NP core to the overall micrometer length of the virus arms makes our hybrid particles a scaled-up system of soft star-like particles, whose components can be directly tracked by optical microscopy. In this paper, we report on the dynamics of an ensemble of virus-based star particles in the dilute regime—where the interparticle interactions are negligible—by means of single particle tracking (SPT) and dynamic light scattering (DLS). Our results show diffusive behavior on long time scales but are also able to resolve the change of dynamics on short time scales due to the internal degrees of freedom of our particles.

RESULTS

We construct our star-like particles via the self-assembly in aqueous solution of 50 nm Au nanoparticles (Au NPs) with micrometer long filamentous rodlike viruses (M13) which are genetically modified to selectively and irreversibly bind to noble metals with one of their tips (see Materials and Methods). This results in a hybrid particle whose Au core is surrounded by a brush formed by about $n \simeq 23$ semiflexible viral arms (Figure 1 and Figure S1 in the Supporting Information). The rigidity of the viral arms whose persistence length is larger than their contour length ($L_p > L_c$, see Materials and Methods) imparts a sea urchin-like morphology to the particles. A key-feature of these isometric particles is their *monodispersity* in diameter, $\sigma_{star} \simeq 2$ μm (Figure 1) stemming from the intrinsic uniformity in size of the viral "spines".[44]

The confocal microscopy images of Figure 1 and the Supplementary Movies show that beyond the Brownian displacement of the particles, their viral arms are also moving. For a better understanding of the star behavior, their dynamics is investigated in the dilute regime by single particle tracking using fluorescence microscopy. Traces are recorded in the observation plane (Figure S2), *i.e.*, nearly in 2D, from which the mean squared displacement (MSD) is calculated (see Materials and Methods for details and Figure S3), as plotted in Figure 2(a). The general expression of the mean squared displacement in n dimensions as a function of time is[48,49]

$$\mathrm{MSD} = 2nD_T t^{\gamma} \quad (1)$$

where D_T is the translational diffusion rate and γ is the diffusivity exponent indicating the nature of the dynamics: subdiffusive for $\gamma < 1$, diffusive for $\gamma = 1$, and superdiffusive for $\gamma > 1$. The linear dependence with time, found for the MSD

https://doi.org/10.1021/acsnano.3c06134
ACS Nano 2024, 18, 281−287

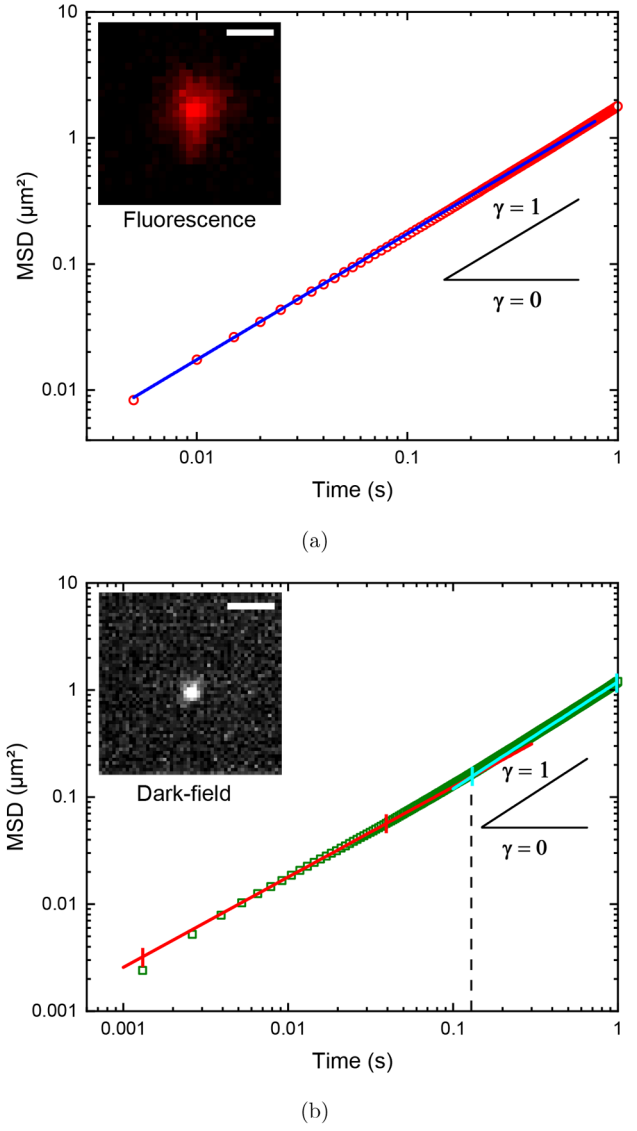

Figure 2. Star particle mean squared displacement (MSD) measured by (a) fluorescence and (b) dark-field microscopy. (a) The blue line is a power-law fit according to eq 1 and indicates a diffusive regime ($\gamma = 1$) over the full range of the times probed, with a diffusion coefficient of $D_T^{Fluo} = 0.43\ \mu m^2/s$. Inset: Fluorescence microscopy image of a star particle obtained during single particle tracking performed for the MSD determination. (b) Dark-field microscopy experiment, where solely the Au core of the star is tracked as shown in the inset. The lines are power-law fits according to eq 1, and indicate two regimes: a diffusive behavior (cyan line, $\gamma = 1$) at long times with a diffusion coefficient $D_T^{DF} = 0.30\ \mu m^2/s$, and a subdiffusive one (red line) with $\gamma = 0.85$ for short times. A crossover time $\tau_{cross} \simeq 130$ ms can be defined between the two regimes, and it is shown by the vertical dashed line. The fit range of each regime is indicated by small colored vertical dashes. In both insets, the scale bar represents 2 μm.

measured by fluorescence (Figure 2(a)), indicates a diffusive regime ($\gamma = 1$) for the star particles, from which the three-dimensional translational diffusion coefficient $D_T^{Fluo} = 0.43\ \mu m^2/s$ can be determined according to eq 1 with $n = 2$.

However, a careful inspection of the tracking by fluorescence microscopy suggests that the measured MSD and therefore D_T^{Fluo} are overestimated because they include a random uncertainty in the determination of the particle center-of-mass, stemming from the motion of the arms, which shifts the maximum fluorescence intensity position from the real particle center-of-mass (see Supporting Information, inset of Figure 2(a), and Figure S4).

To circumvent this problem, we take advantage of the hybrid feature of the stars and specifically that the Au core of the particle exhibits a high scattering signal as observed by dark-field (DF) microscopy. Using this technique, we are able to visualize only the star's metallic core, as the viral organic arms are nearly invisible with this method (see inset of Figure 2(b)). Single particle tracking is then performed, and the high contrast of the Au core revealed by dark-field allows for a significant increase of the frame rate of the acquired movies (see Materials and Methods) giving us access to shorter time scales, *i.e.*, ∼1 ms. The resulting MSD averaged over about 160 traces is shown in Figure 2(b) and Figure S3. Interestingly, two regimes can be distinguished: a diffusive behavior ($\gamma = 1$) at long times from which a diffusion coefficient $D_T^{DF} = 0.30\ \mu m^2/s$ is measured, and a subdiffusive regime with $\gamma \simeq 0.85$. The former regime shows a diffusion coefficient, D_T^{DF}, significantly lower than that measured with fluorescence and confirms *a posteriori* that D_T^{Fluo} is overestimated, whereas the subdiffusivity of the latter regime suggests some hindered motion of the metal core.

For a better picture of what happens within the components of the star and to complete the investigation of the different MSD regimes found in Figure 2(b), we complement the study by using dynamic light scattering (DLS) in the dilute regime of the particle concentration. In DLS as in DF microscopy, the scattering signal of the Au NPs far exceeds that of the viruses. The intensity correlation function, or second-order correlation function, $g_2(q, t)$, is acquired as a function of the scattering wavevector magnitude, q, which is directly related to the scattering angle θ (see eq 4 in Materials and Methods).[50] In the simplest case, *i.e.*, for noninteracting, solid, spherical particles uniform in diameter, $g_2(q, t)$ is a single exponential decay function with decay time, $\tau=(2q^2D_T)^{-1}$, expressed in terms of the self-intermediate scattering function, $F_s(q, t)$, as[51]

$$g_2(q, t)-1 = \beta \exp(-2q^2D_T t)=\beta |F_s(q, t)|^2 \quad (2)$$

where β is the coherence factor, expected to be close to 1 for nearly ideal experimental conditions. The experimental intensity correlation functions $g_2(q, t)$ acquired by DLS are *globally* fitted using eq 2, as shown in Figure S5. A simple inspection of the global fit indicates that eq 2 cannot properly account for the experimental scattering signal of the stars, showing a significant deviation of their dynamics from the standard Brownian motion of noninteracting uniform solid spheres.[51]

This, in combination with the subdiffusive regime of the MSD observed at short times by DF microscopy (Figure 2(b)), suggests that the grafting of viruses to the Au nanoparticle surface inhibits the motion of the Au core around its reference position in the center of the star particle. We propose, therefore, as a description of the internal dynamics of the stars, to model the hindered motion of their core by a Brownian particle trapped in a harmonic potential (spring model).

This process was initially described by Ornstein and Uhlenbeck,[52] and leads to an extra- contribution, F_{int}, to the self-intermediate scattering function F_s (see Materials and

https://doi.org/10.1021/acsnano.3c06134
ACS Nano 2024, 18, 281−287

Methods),[53] related to the intensity correlation function through eq 2

$$g_2(q, t) - 1 = \beta\{\exp(-D_T q^2 t) \times (\exp\{-q^2\langle r_{int}^2\rangle[1 - \exp(-\xi t)]\})\}^2 \quad (3)$$

with $\langle r_{int}^2\rangle = \frac{k_B T}{\kappa}$ the mean square displacement within the harmonic potential at the relaxation time $1/\xi = \gamma_0/\kappa$, written in terms of the friction coefficient, γ_0, and spring constant, κ, associated with the harmonic potential. The *global* fit of the intensity correlation functions at different angles using the spring model (eq 3) is represented by the black lines in Figure 3. It accounts accurately for the experimental scattering signal,

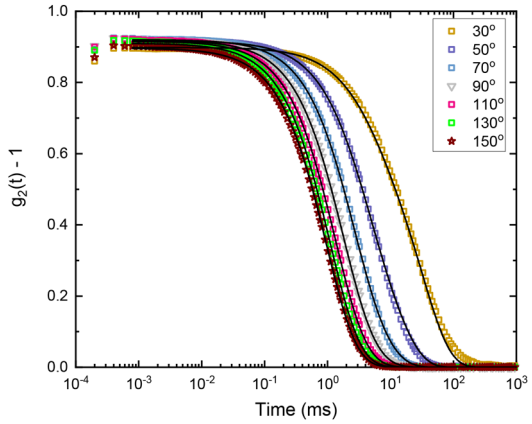

Figure 3. Intensity correlation function $g_2(q,t)$ of star particle suspensions at OD_{520} = 0.15 measured by dynamic light scattering for various scattering angles θ (symbols) from 30° to 150° in steps of 10°. For clarity, only half of the angles, *i.e.*, every 20°, have been plotted. Data are *globally* fitted using the spring model (eq 3) (black lines). The global parameters obtained from the fit are D_T = 0.33 ± 0.02 $\mu m^2/s$, $\langle r_{int}^2\rangle$ = 2.7 ± 0.4 × 10^{-3} μm^2 and ξ = 0.17 ± 0.01 ms^{-1}.

with the following global parameters: D_T = 0.33 ± 0.02 $\mu m^2/s$, $\langle r_{int}^2\rangle$ = 2.7 ± 0.4 × 10^{-3} μm^2 and ξ = 0.17 ± 0.01 ms^{-1}. In order to prove that these results are obtained in the dilute regime where the interactions between particles can be neglected, the same analysis is performed for other dilutions as shown in Figures S6 and S7 for which the fit parameters (see caption of Figures 3, S6, and S7) are found to be independent of the sample dilution.

DISCUSSION

The diffusion coefficient D_T = 0.33 $\mu m^2/s$, obtained by DLS using the Ornstein and Uhlenbeck model is in outstanding agreement with the one determined by SPT, D_T^{DF} = 0.30 $\mu m^2/s$, considering the independence of the two approaches and the number of independent parameters (three, namely D_T, $\langle r_{int}^2\rangle$, and ξ) used for fitting the DLS data.

From that diffusion coefficient, the hydrodynamic radius, R_H, referring to the size of the hard sphere diffusing at the same D_T can be defined as $R_H = k_B T/(6\pi\eta D_T)$, with η being the viscosity of water, and is found to be R_H = 0.65 μm. Such a value is lower than the star geometric radius or equivalently to the virus contour length, *i.e.*, $R_H < \sigma_{star}/2 \simeq L_c$ = 1 μm, a result which is expected in view of the fuzziness and loose morphology of the particles compared to a solid sphere.

Two other physical parameters can be extracted from the global fit (see previous section and Figure 3) using the Ornstein and Uhlenbeck model: (1) the mean square displacement $\langle r_{int}^2\rangle = \frac{k_B T}{\kappa}$ within the harmonic potential, from which the spring constant can be directly deduced, κ = 370 $k_B T/\mu m^2$; and (2) the relaxation time $1/\xi = \gamma_0/\kappa$, which allows for the determination of the friction coefficient, γ_0 = 2.2 $k_B T$ s/μm^2. The Stokes radius, R_S, corresponding to the size of a spherical dense colloid having the same friction $\gamma_0 = 6\pi\eta R_S$ and which is therefore conceptually equivalent to a hydrodynamic radius, is found to be R_S = 0.48 μm. This value derived from the second and third fitting parameters is smaller by about 26% than the hydrodynamic radius R_H derived from the first fitting parameter. While R_H is associated with the motion of the entire star in aqueous solvent, R_S is related to the internal dynamics of the particle and the displacement of the core in the crowded environment of viruses.

As a consequence, our modeling shows that the star particles exhibit internal degrees of freedom, which can stem from the tip proteins p3 used for binding the viruses to the Au NPs and acting as entropic springs, as well as from the flexibility of the whole phages quantified by their persistence length L_p. In the latter case, the phage effective length or end-to-end length L is a function of both the contour length L_c and the persistence length L_p, which leads to L = 0.94 μm according to the Kratky and Porod relation[54] for isolated polymer chains. The difference between the phage contour length and effective length $L_c - L \simeq$ 60 nm is consistent with the typical length scale obtained from the root-mean-square displacement $\sqrt{r_{int}^2}$ ~52 nm (Figure 3). However, visual inspection of the Supplementary Movie acquired by fluorescence microscopy reveals that the viral arms have a significant angular motion beyond the rotational diffusion of the full particle, which suggests a more localized flexibility associated with the tip proteins p3 linking the M13 virus to the Au NP. The flexibility of the p3 tip protein is consistent with its biological structure comprising 406 amino acids formed by three domains (N1, N2, and C) separated by soft flexible glycine-rich linkers.[55] These glycine-rich linkers result in the spreading of p3 away from the virus body and the presence of knobs as seen in electron micrographs,[56] and they provide to the protein its ability for conformational change. Moreover, the elastic and structural flexibility of p3 has been recently shown to play a major role in the infection of the bacterial host.[57] In its standard configuration, as used here, the spatial extension of the five p3 tip proteins far exceeds the 7 nm of the virus diameter and has been found to be around $l \sim$ 20 nm, enabling a high accessibility.[56,57] The corresponding footprint of the p3 proteins can then be estimated by $\pi(l/2)^2$ and be compared with the area available on the Au NP surface (neglecting curvature effect): πd_{Au}^2 with d_{Au} = 51 nm. The ratio between these two areas provides an estimation of the highest number of viral arms that can be grafted to the nanoparticle surface, $n_{max} \simeq$ 26, very close to the average valency $n \simeq$ 23 found experimentally (Figure 1 and Figure S1).

CONCLUSION

In this work, we have produced and studied the dynamics in the dilute regime of virus-based hybrid soft monodisperse star particles. Taking advantage of the optical contrast between the metallic Au core and the viral arms, we have shown thanks to

https://doi.org/10.1021/acsnano.3c06134
ACS Nano 2024, 18, 281−287

optical microscopy and dynamic light scattering that, beyond their overall Brownian diffusion, these stars exhibit internal degrees of freedom, which can stem both from the flexibility of the whole phage and from the virus tip proteins acting as entropic springs. A flexible link is evidenced between the virus body and the metallic core formed by the Au nanoparticle, whose dynamics can be accounted for by a spring model, *i.e.*, a Brownian particle trapped in a harmonic potential. The internal flexibility of the star particles combined with their sparse morphology make this system very appealing for probing the dense regimes and investigating their mutual interactions, potentially leading to dynamical arrest in glassy or jammed states.

MATERIAL AND METHODS

Hybrid Virus-Based Star Particles. The star particles are produced by self-assembly in a solution of tannic-acid-stabilized Au (NPs) of diameter d_{Au} = 51 ± 6 nm (NanoComposix, Inc.) with genetically modified rod-shaped viruses, named M13C7C. The M13C7C virus mutant, obtained from the commercially available phage display peptide library kit (New England Biolabs), is a *monodisperse* filamentous bacteriophage of contour length L_c = 1 μm and diameter d = 7 nm. This negatively charged polyelectrolyte is semirigid with a persistence length, L_p, exceeding its contour length, *i.e.*, $L_p \simeq 3L_c$.[58] The 5 copies of the tip protein p3 displayed at the proximal end of the virus are genetically modified with the fusion of the following amino-acid sequence before the N-terminal amine and therefore exposed to the solvent: GGGCTAERVPDCA-NH2.[59] The two cysteine residues, C, present solely at one of the virus ends, and otherwise absent from the capsid, are thiol-containing amino acids, forming disulfide bridges which enable selective binding to noble metals via a dative bond.[60] Both components of the stars are initially mixed with the virus mutants in a molar excess of about 100 per Au NP. To promote the star formation by grafting the virus tips to the Au NPs, the electrostatic repulsion between Au NPs and viruses is screened stepwise by dialyzing the suspension against Tris/HCl/NaCl buffers at pH 8.2 in a range of ionic strength from I = 20 to 200 mM by adjusting the amount of NaCl. This results in star-like particles with viral arms linked by one tip to a solid metal core (Figure 1).[44,61] The excess of viruses is removed by typically three centrifugation steps at 4000*g* for 30 min: the stars are collected in the pellet before being redispersed, whereas the supernatant containing the nonreacted viruses is discarded. After purification, hybrid virus-based star particles are obtained, as observed by transmission electron microscopy in Figure 1 and Figure S1, from which the distribution of arms, and therefore the average valency, $\langle n \rangle$ = 23 ± 6 viruses per Au NP, is measured. The fluorescent structures are prepared following the same protocol but with a batch of M13C7C previously labeled with red fluorescent dyes (Dylight 550-NHS ester, Thermo Scientific) according to a procedure reported elsewhere.[44] Using the plasmonic resonance of the Au core at λ_{Au} = 520 nm, the particle concentration of the hybrid virus-based stars is determined by $C_{star} = C_{AuNP} = OD_{520}N_A/(l \times \varepsilon_{520})$, where OD_{520} is the optical absorption, N_A is Avogadro's number, l is the optical path and ε_{520} = 1.94 × 10^{10} $M^{-1}cm^{-1}$ is the Au NP molar extinction coefficient.[62]

Transmission Electron Microscopy (TEM). Suspensions with typical concentrations C_{star} = 1.6 × 10^9 stars/mL are used to prepare samples for TEM on O_2 plasma-treated carbon-coated grids then negatively stained with 2% uranyl acetate to reveal the organic viruses. An AMT CCD camera mounted on a Hitachi H-600 electron microscope operating at 75 kV is used to observe the grids and record the images.

Optical Microscopy and Single Particle Tracking (SPT). Suspensions of stars of respective optical density OD_{520} = 0.05 (*i.e.*, C_{star} = 1.6 × 10^9 stars/mL) for fluorescence and confocal microscopy, and OD_{520} = 0.03 (*i.e.*, C_{star} = 9 × 10^8 stars/mL) for dark-field microscopy, are prepared in Tris/HCl/NaCl buffer (I = 100 mM, pH 8.2) and set in optical cells whose thickness is between 10 and 15 μm. The microscopy cells are composed by a coverslip and a glass slide, first cleaned with sulfochromic acid, and sealed by ultraviolet-cured glue (NOA81, Epotecny). Confocal fluorescence microscopy images are recorded with a Zeiss LSM 980 microscope at a frame rate of 35 fps. The dark-field (DF) observations are performed using an inverted microscope equipped with an Olympus UPlanFLN 100× oil-immersion objective of adjustable numerical aperture (NA) from 0.6 to 1.3, and an Olympus U-DCW oil-immersion dark-field condenser (NA = 1.2−1.4). The same microscope, equipped with an Omicron LedHub as a light source, is used for fluorescence observation, where the objective is a 100× oil-immersion PlanAPO of high numerical aperture, NA = 1.4. Images are acquired with an ultrafast electron-multiplying camera (NEO sCMOS Andor) having a pixel size of 6.5 μm. The dynamics of the system is obtained using single particle tracking (SPT) in wide-field microscopy, where we measure the two-dimensional projection of the isotropic Brownian trajectories in the objective focal plane.[48,63,64] The experimental conditions are optimized to get the highest frame rate possible with a signal-to-noise ratio sufficient for good detection. Thanks to the high scattering signal of the Au NPs, a frame rate of 762 fps was applied for dark-field microscopy. It decreased to 199 fps for fluorescence microscopy, whose signal-to-noise ratio is intrinsically lower. Two-dimensional traces $r(t)$ are collected using a custom-written particle tracking algorithm developed in MATLAB (MathWorks) (Figure S2). The mean squared displacement defined as MSD = $\langle r^2(t) \rangle$, is calculated for each trace (Figure S3), before being first averaged over the total number of detected particles and then fitted to determine the corresponding diffusion coefficient according to eq 1 with n = 2.[63] The number of valid collected traces acquired for each contrast mode is N_{star} = 160 and 151 for the dark-field and fluorescence microscopy techniques, respectively (Figure S3). This high number of traces, N_{star} > 100, allows for an accurate estimation of the diffusion coefficients with an error bar of less than 5%.[64] We cutoff our fitting range (Figure 2 and Figure S3) because of the limitation on tracking particles for long times (larger than 1 s).

Dynamic Light Scattering (DLS). Three samples having star concentration of OD_{520} = 0.15 (*i.e.*, C_{star} = 4.7 × 10^9 stars/mL) in I = 0.5 mM pH 8.2 Tris-HCl buffer, as well as OD_{520} = 0.05 (*i.e.*, C_{star} = 1.6 × 10^9 stars/mL) and OD_{520} = 0.17 (*i.e.*, C_{star} = 5.3 × 10^9 stars/mL) in I = 100 mM pH 8.2 Tris-HCl-NaCl buffer, are prepared by dialysis and then transferred into a light scattering glass tube of 10 mm diameter. The tube is immersed in a bath of toluene for index matching, and regulated at a constant temperature of T = 20 °C. The time-intensity correlation function, $g_2(q, t)$, of the scattered light is recorded in the polarized (*i.e.*, VV) geometry[51] using an ALV laser goniometer with a HeNe linearly polarized laser of λ_L = 632.8 nm and an ALV500/EPP digital correlator (ALV-GmbH Technology). The scattering angle, θ, is varied from 30° to 150° in steps of 10°, which allows us to probe a range of scattering wavevectors

$$q = \frac{4\pi n_0}{\lambda_L}\sin(\theta/2) \tag{4}$$

from 6.8 × 10^{-3} $nm^{-1} \leq q \leq$ 2.55 × 10^{-2} nm^{-1}, where n_0 is the refractive index of the solvent—here, water.[51] The 13 scattered intensity correlation functions $g_2(q, t)$ covering the full range of scattering angles are then globally (*i.e., not* independently) fitted with eq 2 using OriginPro 2020 (Originlab Corporation) software, accounting for the basic Brownian diffusion of spherical particles, or with eq 3. The latter is derived from the decoupling approximation of the intermediate scattering function in which $F_s(q, t)$ includes contributions from the overall translational (trans) and rotational (rot) diffusions as well as from internal dynamics of the particle, which can be modeled by a constrained Brownian motion within a harmonic potential as described by Ornstein and Uhlenbeck:[52,53]

$$F_s(q, t) = F_{trans}(q, t)\cdot F_{rot}(q, t)\cdot F_{int}(q, t) \tag{5}$$

with $F_{trans}(q, t)$ and $F_{rot}(q, t)$ the translational and rotational contributions to the intermediate scattering function, respectively, and

https://doi.org/10.1021/acsnano.3c06134
ACS Nano 2024, 18, 281−287

$$F_{int} = \exp\{-q^2\langle r_{int}^2\rangle[1-\exp(-\xi t)]\} \quad (6)$$

is the contribution due to the internal dynamics (spring model).[53] Different parameters characterize these internal degrees of freedom: $\langle r_{int}^2\rangle = \frac{k_B T}{\kappa}$, with k_B being the Boltzmann constant and T the temperature, is the mean square displacement within the harmonic potential at the relaxation time $1/\xi = \gamma_0/\kappa$, written in terms of the friction coefficient, γ_0, and spring constant, κ. Considering that the NPs being probed are nearly spherical, we approximate the first two factors of eq 5 to the intermediate scattering function of monodisperse isotropic particles[51]

$$F_{trans}(q, t)\cdot F_{rot}(q, t) \approx F_{sphere}(q, t) = \exp(-q^2 D_T t) \quad (7)$$

Combining eqs 5, 6, and 7, and applying the relation between $F_s(q, t)$ and $g_2(q, t)$ given by eq 2, we obtain the final expression of eq 3, which is used to globally fit the experimental data, as shown in Figure 3 by black lines.

ASSOCIATED CONTENT

Supporting Information

The Supporting Information is available free of charge at https://pubs.acs.org/doi/10.1021/acsnano.3c06134.

Electron microscopy images and valency of star particles; traces obtained from single particle tracking and corresponding MSD of stars; DLS data and fitting with uniform sphere model and with the spring model at different dilutions; model of the random displacement of the apparent center-of-mass (PDF)

Confocal microscopy movie of star particles (AVI)

Fluorescence microscopy movie of star particles (AVI)

AUTHOR INFORMATION

Corresponding Author

Eric Grelet − *Univ. Bordeaux, CNRS, Centre de Recherche Paul-Pascal, F-33600 Pessac, France;* orcid.org/0000-0002-9645-7077; Email: eric.grelet@crpp.cnrs.fr

Author

Arantza B. Zavala-Martínez − *Univ. Bordeaux, CNRS, Centre de Recherche Paul-Pascal, F-33600 Pessac, France*

Complete contact information is available at: https://pubs.acs.org/10.1021/acsnano.3c06134

Author Contributions

A.B.Z.-M. prepared the samples and the first version of the manuscript, performed the experiments, collected and analyzed the data. E.G. devised the study, supervised the project, analyzed and interpreted the data, wrote, revised, and edited the manuscript.

Notes

The authors declare no competing financial interest.

ACKNOWLEDGMENTS

We thank F. Nallet for his interest in this work. We acknowledge financial support from the French National Research Agency (ANR) under grant No. ANR-21-CE06-0045-StarRAC.

REFERENCES

(1) Vincent, B.; Edwards, J.; Emmett, S.; Jones, A. Depletion Flocculation in Dispersions of Sterically-Stabilised Particles ("Soft Spheres"). *Colloids Surf.* **1986**, *18*, 261−281.

(2) Likos, C. N. Soft Matter with Soft Particles. *Soft Matter* **2006**, *2*, 478−498.

(3) Vlassopoulos, D.; Cloitre, M. Tunable Rheology of Dense Soft Deformable Colloids. *Curr. Opin. Colloid Interface Sci.* **2014**, *19*, 561−574.

(4) Wei, G.; Zhao, C.; Hollingsworth, J.; Zhou, Z.; Jin, F.; Zhang, Z.; Cheng, H.; Han, C. C. Mechanism of Two-Dimensional Crystal Formation from Soft Microgel Particles. *Soft Matter* **2013**, *9*, 9924.

(5) Lindenblatt, G.; Schärtl, W.; Pakula, T.; Schmidt, M. Synthesis of Polystyrene-Grafted Polyorganosiloxane Microgels and Their Compatibility with Linear Polystyrene Chains. *Macromolecules* **2000**, *33*, 9340−9347.

(6) Eckert, T.; Richtering, W. Thermodynamic and Hydrodynamic Interaction in Concentrated Microgel Suspensions: Hard or Soft Sphere Behavior? *J. Chem. Phys.* **2008**, *129*, 124902.

(7) Laurati, M.; Stellbrink, J.; Lund, R.; Willner, L.; Richter, D.; Zaccarelli, E. Starlike Micelles with Starlike Interactions: A Quantitative Evaluation of Structure Factors and Phase Diagram. *Phys. Rev. Lett.* **2005**, *94*, 195504.

(8) Merlet-Lacroix, N.; Di Cola, E.; Cloitre, M. Swelling and Rheology of Thermoresponsive Gradient Copolymer Micelles. *Soft Matter* **2010**, *6*, 984.

(9) Erwin, B. M.; Cloitre, M.; Gauthier, M.; Vlassopoulos, D. Dynamics and Rheology of Colloidal Star Polymers. *Soft Matter* **2010**, *6*, 2825−2833.

(10) Gupta, S.; Camargo, M.; Stellbrink, J.; Allgaier, J.; Radulescu, A.; Lindner, P.; Zaccarelli, E.; Likos, C. N.; Richter, D. Dynamic Phase Diagram of Soft Nanocolloids. *Nanoscale* **2015**, *7*, 13924−13934.

(11) Gury, L.; Gauthier, M.; Cloitre, M.; Vlassopoulos, D. Colloidal Jamming in Multiarm Star Polymer Melts. *Macromolecules* **2019**, *52*, 4617−4623.

(12) Pusey, P. N.; van Megen, W. Phase Behaviour of Concentrated Suspensions of Nearly Hard Colloidal Spheres. *Nature* **1986**, *320*, 340−342.

(13) Tokuyama, M.; Oppenheim, I. Dynamics of Hard-Sphere Suspensions. *Phys. Rev. E* **1994**, *50*, R16.

(14) Pusey, P. N.; Tough, R. J. Hydrodynamic Interactions and Diffusion in Concentrated Particle Suspensions. *Faraday Discuss. Chem. Soc.* **1983**, *76*, 123−136.

(15) van Megen, W.; Underwood, S. M.; Pusey, P. N. Dynamics of Hard Spherical Colloids from the Fluid to the Glass. *J. Chem. Soc., Faraday Trans.* **1991**, *87*, 395−401.

(16) Vlassopoulos, D.; Cloitre, M. *Theory and Applications of Colloidal Suspension Rheology*; Cambridge University Press Cambridge, 2021; pp 227−290.

(17) De Gennes, P.; Leger, L. Dynamics of Entangled Polymer Chains. *Annu. Rev. Phys. Chem.* **1982**, *33*, 49−61.

(18) Chu, B.; Wang, Z.; Yu, J. Dynamic Light Scattering Study of Internal Motions of Polymer Coils in Dilute Solution. *Macromolecules* **1991**, *24*, 6832−6838.

(19) Romeo, G.; Imperiali, L.; Kim, J.-W.; Fernández-Nieves, A.; Weitz, D. A. Origin of De-Swelling and Dynamics of Dense Ionic Microgel Suspensions. *J. Chem. Phys.* **2012**, *136*, 124905.

(20) Freedman, K. O.; Lee, J.; Li, Y.; Luo, D.; Skobeleva, V. B.; Ke, P. C. Diffusion of Single Star-Branched Dendrimer-Like DNA. *J. Phys. Chem. B* **2005**, *109*, 9839−9842.

(21) Cautela, J.; Stenqvist, B.; Schillén, K.; Belić, D.; Månsson, L. K.; Hagemans, F.; Seuss, M.; Fery, A.; Crassous, J. J.; Galantini, L. Supracolloidal Atomium. *ACS Nano* **2020**, *14*, 15748−15756.

(22) Gasser, U.; Hyatt, J. S.; Lietor-Santos, J.-J.; Herman, E. S.; Lyon, L. A.; Fernandez-Nieves, A. Form Factor of pNIPAM Microgels in Overpacked States. *J. Chem. Phys.* **2014**, *141*, 034901.

(23) Laurati, M.; Stellbrink, J.; Lund, R.; Willner, L.; Richter, D.; Zaccarelli, E. Starlike Micelles with Starlike Interactions: A Quantitative Evaluation of Structure Factors and Phase Diagram. *Phys. Rev. Lett.* **2005**, *94*, 195504.

(24) Fleischer, G.; Fytas, G.; Vlassopoulos, D.; Roovers, J.; Hadjichristidis, N. Self-Diffusion of Multiarm Star Polymers in

Solution Far from and near the Ordering Transition. *Phys. A (Amsterdam, Neth.)* **2000**, *280*, 266−278.
(25) Mattsson, J.; Wyss, H. M.; Fernandez-Nieves, A.; Miyazaki, K.; Hu, Z.; Reichman, D. R.; Weitz, D. A. Soft Colloids Make Strong Glasses. *Nature* **2009**, *462*, 83−86.
(26) Conley, G. M.; Aebischer, P.; Nöjd, S.; Schurtenberger, P.; Scheffold, F. Jamming and Overpacking Fuzzy Microgels: Deformation, Interpenetration, and Compression. *Sci. Adv.* **2017**, *3*, No. e1700969.
(27) Zhang, J.; Lettinga, P. M.; Dhont, J. K. G.; Stiakakis, E. Direct Visualization of Conformation and Dense Packing of DNA-Based Soft Colloids. *Phys. Rev. Lett.* **2014**, *113*, 268303.
(28) Romero-Sanchez, I.; Pihlajamaa, I.; Adžić, N.; Castellano, L. E.; Stiakakis, E.; Likos, C. N.; Laurati, M. Blunt-End Driven Re-entrant Ordering in Quasi Two-Dimensional Dispersions of Spherical DNA Brushes. *ACS Nano* **2022**, *16*, 2133−2146.
(29) Buitenhuis, J.; Förster, S. Block Copolymer Micelles: Viscoelasticity and Interaction Potential of Soft Spheres. *J. Chem. Phys.* **1997**, *107*, 262−272.
(30) Vlassopoulos, D.; Fytas, G.; Pakula, T.; Roovers, J. Multiarm Star Polymers Dynamics. *J. Phys.: Condens. Matter* **2001**, *13*, R855−R876.
(31) Cloitre, M., Ed. High Solid Dispersions; *Adv. Polym. Sci.*; Springer Berlin Heidelberg, 2010; Vol. *236*.
(32) Choi, J.; Hui, C. M.; Pietrasik, J.; Dong, H.; Matyjaszewski, K.; Bockstaller, M. R. Toughening Fragile Matter: Mechanical Properties of Particle Solids Assembled from Polymer -Grafted Hybrid Particles Synthesized by ATRP. *Soft Matter* **2012**, *8*, 4072−4082.
(33) Shay, J. S.; Raghavan, S. R.; Khan, S. A. Thermoreversible Gelation in Aqueous Dispersions of Colloidal Particles Bearing Grafted Poly (Ethylene Oxide) Chains. *J. Rheol.* **2001**, *45*, 913−927.
(34) Ohno, K.; Morinaga, T.; Takeno, S.; Tsujii, Y.; Fukuda, T. Suspensions of Silica Particles Grafted with Concentrated Polymer Brush: a New Family of Colloidal Crystals. *Macromolecules* **2006**, *39*, 1245−1249.
(35) Ohno, K.; Morinaga, T.; Takeno, S.; Tsujii, Y.; Fukuda, T. Suspensions of Silica Particles Grafted with Concentrated Polymer Brush: Effects of Graft Chain Length on Brush Layer Thickness and Colloidal Crystallization. *Macromolecules* **2007**, *40*, 9143−9150.
(36) Tricot, M. Chain Flexibility Parameter and Persistence Length of Various Poly (Methacrylic Acid Esters). *Macromolecules* **1986**, *19*, 1268−1270.
(37) Lee, H.; Venable, R. M.; MacKerell, A. D.; Pastor, R. W. Molecular Dynamics Studies of Polyethylene Oxide and Polyethylene Glycol: Hydrodynamic Radius and Shape Anisotropy. *Biophys. J.* **2008**, *95*, 1590−1599.
(38) Biffi, S.; Cerbino, R.; Bomboi, F.; Paraboschi, E. M.; Asselta, R.; Sciortino, F.; Bellini, T. Phase Behavior and Critical Activated Dynamics of Limited-Valence DNA Nanostars. *Proc. Natl. Acad. Sci. U.S.A.* **2013**, *110*, 15633−15637.
(39) Rovigatti, L.; Smallenburg, F.; Romano, F.; Sciortino, F. Gels of DNA Nanostars Never Crystallize. *ACS Nano* **2014**, *8*, 3567−3574.
(40) Brady, R. A.; Brooks, N. J.; Cicuta, P.; Di Michele, L. Crystallization of Amphiphilic DNA C-Stars. *Nano Lett.* **2017**, *17*, 3276−3281.
(41) Lattuada, E.; Pietrangeli, T.; Sciortino, F. Interpenetrating Gels in Binary Suspensions of DNA Nanostars. *J. Chem. Phys.* **2022**, *157*, 135101.
(42) Lu, Y.; Weers, B.; Stellwagen, N. C. DNA Persistence Length Revisited. *Biopolymers* **2002**, *61*, 261−275.
(43) Brady, R. A.; Kaufhold, W. T.; Brooks, N. J.; Foderà, V.; Di Michele, L. Flexibility Defines Structure in Crystals of Amphiphilic DNA Nanostars. *J. Phys.: Condens. Matter* **2019**, *31*, 074003.
(44) de la Cotte, A.; Wu, C.; Trevisan, M.; Repula, A.; Grelet, E. Rod-Like Virus-Based Multiarm Colloidal Molecules. *ACS Nano* **2017**, *11*, 10616−10622.
(45) Zhan, S.; Fang, H.; Chen, Q.; Xiong, S.; Guo, Y.; Huang, T.; Li, X.; Leng, Y.; Huang, X.; Xiong, Y. M13 Bacteriophage as Biometric Component for Orderly Assembly of Dynamic Light Scattering Immunosensor. *Biosens. Bioelectron.* **2022**, *217*, 114693.
(46) Mosquera, J.; García, I.; Henriksen-Lacey, M.; Martínez-Calvo, M.; Dhanjani, M.; Mascareñas, J. L.; Liz-Marzán, L. M. Reversible Control of Protein Corona Formation on Gold Nanoparticles Using Host−Guest Interactions. *ACS Nano* **2020**, *14*, 5382−5391.
(47) Song, L.; Kim, U.-S.; Wilcoxon, J.; Schurr, J. M. Dynamic Light Scattering from Weakly Bending Rods: Estimation of the Dynamic Bending Rigidity of the M13 Virus. *Biopolymers* **1991**, *31*, 547−567.
(48) Crocker, J.; Grier, D. G. Methods of Digital Video Microscopy for Colloidal Studies. *J. Colloid Interface Sci.* **1996**, *179*, 298−310.
(49) Alvarez, L.; Lettinga, M. P.; Grelet, E. Fast Diffusion of Long Guest Rods in a Lamellar Phase of Short Host Particles. *Phys. Rev. Lett.* **2017**, *118*, 178002.
(50) Stetefeld, J.; McKenna, S. A.; Patel, T. R. Dynamic Light Scattering: a Practical Guide and Applications in Biomedical Sciences. *Biophys. Rev.* **2016**, *8*, 409−427.
(51) Berne, B. J.; Pecora, R. *Dynamic light scattering. With applications to chemistry, biology, and physics*; Courier Corporation, 2000.
(52) Uhlenbeck, G. E.; Ornstein, L. S. On the Theory of the Brownian Motion. *Phys. Rev.* **1930**, *36*, 823−841.
(53) Stingaciu, L. R.; Ivanova, O.; Ohl, M.; Biehl, R.; Richter, D. Fast Antibody Fragment Motion: Flexible Linkers Act As Entropic Spring. *Sci. Rep.* **2016**, *6*, 1−13.
(54) Kratky, O.; Porod, G. Röntgenuntersuchung Gelöster Fadenmoleküle. *Recl. Trav. Chim. Pays-Bas* **1949**, *68*, 1106−1122.
(55) Marvin, D. A.; Symmons, M. F.; Straus, S. K. Structure and Assembly of Filamentous Bacteriophages. *Prog. Biophys. Mol. Biol.* **2014**, *114*, 80−122.
(56) Gray, C. W.; Brown, R.; Marvin, D. Adsorption Complex of Filamentous fd Virus. *J. Mol. Biol.* **1981**, *146*, 621−627.
(57) Conners, R.; León-Quezada, R. I.; McLaren, M.; Bennett, N. J.; Daum, B.; Rakonjac, J.; Gold, V. A. M. Cryo-Electron Microscopy of the f1 Filamentous Phage Reveals Insights Into Viral Infection and Assembly. *Nat. Commun.* **2023**, *14*, 2724.
(58) Barry, E.; Beller, D.; Dogic, Z. A Model Liquid Crystalline System Based on Rodlike Viruses with Variable Chirality and Persistence Length. *Soft Matter* **2009**, *5*, 2563−2570.
(59) Repula, A.; Oshima Menegon, M.; Wu, C.; van der Schoot, P.; Grelet, E. Directing Liquid Crystalline Self-Organization of Rodlike Particles through Tunable Attractive Single Tips. *Phys. Rev. Lett.* **2019**, *122*, 128008.
(60) Hermanson, G. T. *Bioconjugate Techniques*, 2nd ed.; Academic Press, 2008.
(61) Huang, F.; Addas, K.; Ward, A.; Flynn, N. T.; Velasco, E.; Hagan, M. F.; Dogic, Z.; Fraden, S. Pair Potential of Charged Colloidal Stars. *Phys. Rev. Lett.* **2009**, *102*, 108302.
(62) Liu, X.; Atwater, M.; Wang, J.; Huo, Q. Extinction Coefficient of Gold Nanoparticles with Different Sizes and Different Capping Ligands. *Colloids Surf., B* **2007**, *58*, 3−7.
(63) Shen, H.; Tauzin, L. J.; Baiyasi, R.; Wang, W.; Moringo, N.; Shuang, B.; Landes, C. F. Single Particle Tracking: From Theory to Biophysical Applications. *Chem. Rev.* **2017**, *117*, 7331−7376.
(64) Novotný, F.; Pumera, M. Nanomotor Tracking Experiments at the Edge of Reproducibility. *Sci. Rep.* **2019**, *9*, 13222.

https://doi.org/10.1021/acsnano.3c06134
ACS Nano 2024, 18, 281−287

Supplementary Information:

M13-phage-based star-shaped particles with internal flexibility

Arantza B. Zavala-Martínez and Eric Grelet*

Univ. Bordeaux, CNRS, Centre de Recherche Paul-Pascal, UMR 5031,

115 Avenue du Dr. Schweitzer, F-33600 Pessac, France

* Corresponding author. E-mail: eric.grelet@crpp.cnrs.fr

Random displacement of the apparent center-of-mass

The tracking of the center-of-mass of the stars is achieved using a 2D-Gaussian fit in order to determine the maximum intensity of the tracked particle in the observation plan. This results in a subpixel resolution in the determination of the particle localization [63]. However, due to the motion of the virus arms, the center-of-mass of the particle usually does not match with the position of the maximum intensity as illustrated in Fig. 1. This mismatch results in an *anisotropic* fluorescence signal, as shown in the Inset of Fig. 2(a) and in Supplementary Fig. S4. The shift $\mathbf{r_s}$ between the real center of mass of the particle and the effective one stemming from contribution of the motion of the arms, is assumed to move as a random walker, therefore its displacement follows a Gaussian probability density. This therefore induces an additional linear contribution to the MSD, which is added to the intrinsic Brownian motion of the particle center-of-mass.

$$G(\mathbf{r_s}, t) = \frac{1}{(4\pi D_s t)^{1/2}} \exp\left(-\frac{{\mathbf{r_s}}^2}{4D_s t}\right) \tag{1}$$

$$\langle {\mathbf{r_s}}^2(t)\rangle = \int d\mathbf{r_s} G(\mathbf{r_s}, t){\mathbf{r_s}}^2 = 4D_s t \tag{2}$$

In brief, the MSD measured by fluorescence microscopy, and therefore the corresponding diffusion coefficient, are overestimated because it includes a random uncertainty in the determination of the particle center-of-mass.

Experimentally, the diffusion coefficient D_T^{Fluo} measured by fluorescence is indeed higher than the one D_T^{DF} obtained by dark-field microscopy, and the difference $\Delta D = D_T^{Fluo} - D_T^{DF} \simeq 0.13\mu\text{m}^2/\text{s}$. The typical shift $\mathbf{r_s}$ between two consecutive frames of exposure time $\tau_0 = 1/\text{fps}$ can then be estimated by $\mathbf{r_s} \simeq (\Delta D \times \tau_0)^{0.5} = 25$ nm, which corresponds to a fraction of the effective pixel size of the camera using $100\times$ magnification (see Materials and Methods) and is consistent with the sub-diffraction limit of the particle localization [63].

Supplementary movies

Confocal and fluorescence microscopy movies of star particles showing their Brownian diffusion and the motion of their viral arms.

Supplementary figures

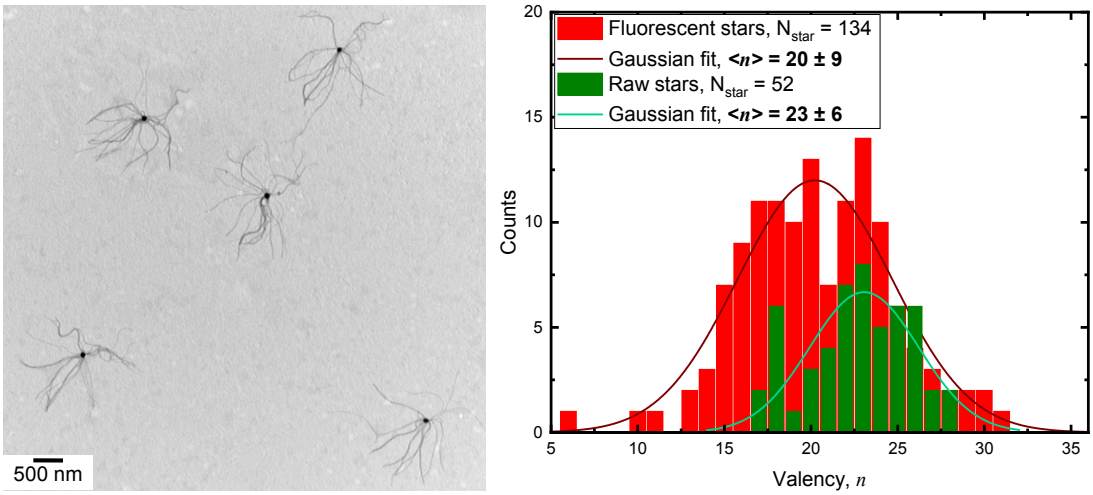

FIG. S1. **Number of virus arms or valency n per star particle. Left:** Large-field-of-view TEM image of star particles. **Right:** Distribution of valencies for the raw (green) and fluorescent (red) stars from which the average valency $\langle n \rangle$ can be obtained by a Gaussian fit (solid lines). N_{star} is the total number of star particles analyzed by TEM.

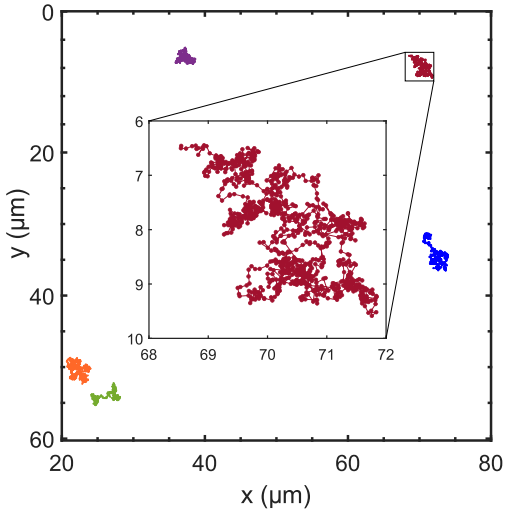

FIG. S2. **Representative trajectories obtained by SPT** with fluorescence microscopy. Since the suspension is in a very dilute regime, only a few particles are within the region of interest. Inset: zoomed-in of trace, illustrating the Brownian diffusion of the particle.

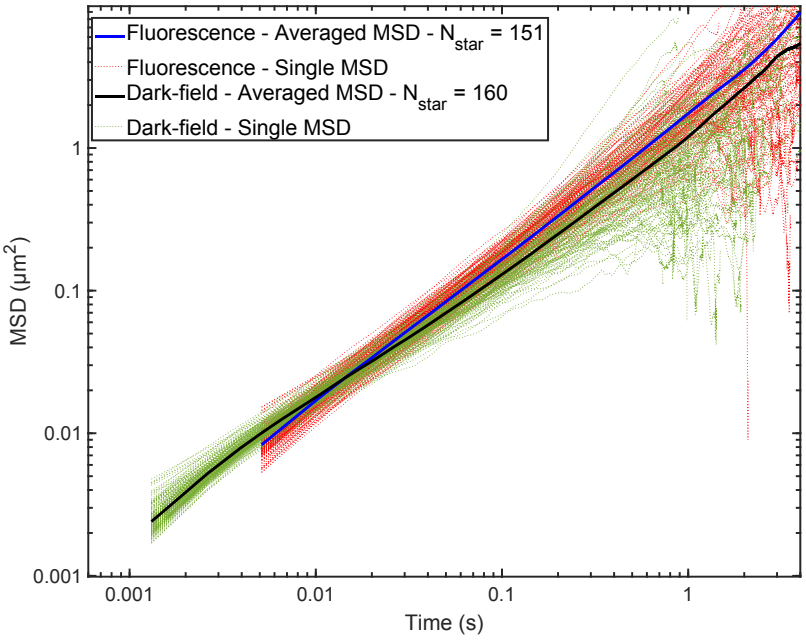

FIG. S3. **Population mean squared displacement** (dotted lines) calculated from each trace obtained by either fluorescence (red) or dark-field (green) microscopy. The solid lines correspond to the averaged MSD over all traces for each microscopy contrast mode.

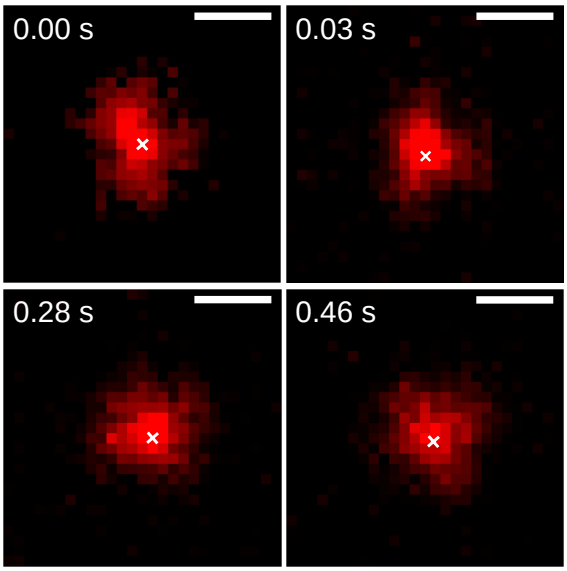

FIG. S4. **Single particle tracking of virus-based stars** using fluorescence microscopy. Snapshots of a single star particle at different times where the maximum light intensity determined during the tracking is indicated with a cross.

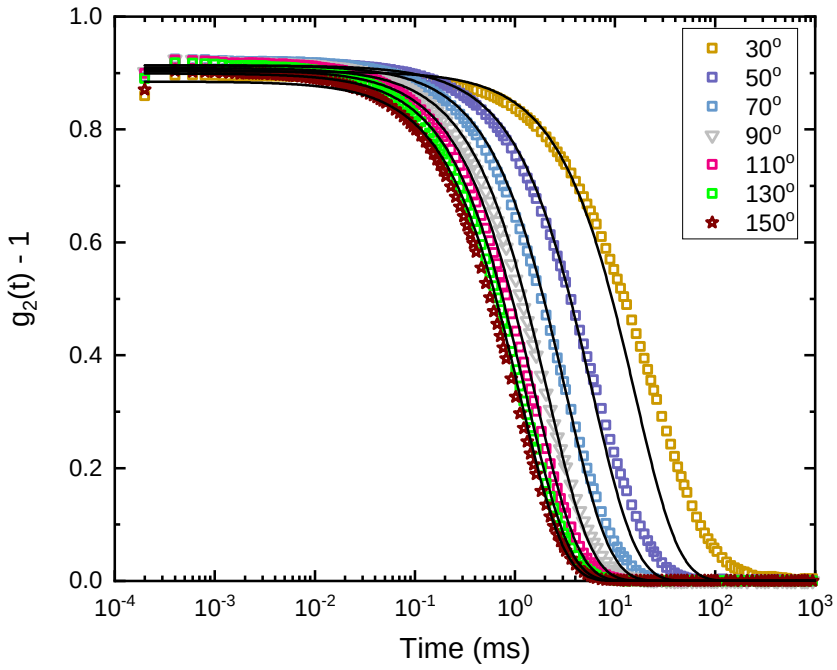

FIG. S5. **Intensity correlation function $g_2(q,t)$ of star particle suspensions at $\mathbf{OD_{520} = 0.15}$ measured by dynamic light scattering** (DLS) for various scattering angles θ (symbols) from 30° to 150° in steps of 10°. For clarity, only half of the angles, *i.e.* every 20°, have been plotted. Global fit is performed using Eq. 2 for Brownian spherical hard particles (black lines), which is not able to accurately account for the experimental data.

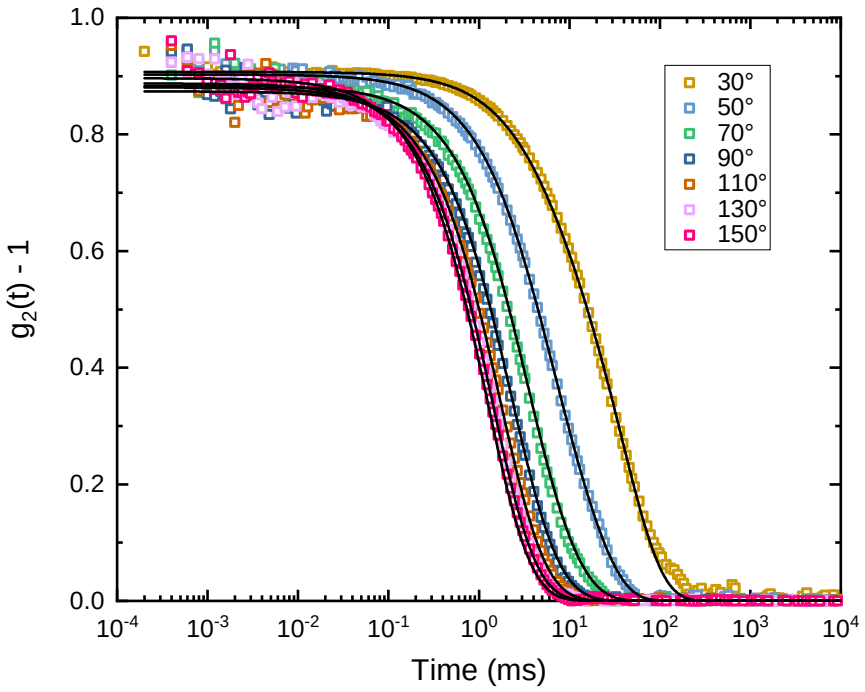

FIG. S6. **Intensity correlation function $g_2(q,t)$ of star particle suspensions at $\mathbf{OD_{520} = 0.05}$ measured by dynamic light scattering** for various scattering angles θ (symbols) from 30° to 150° in steps of 10°. For clarity, only half of the angles, *i.e.* every 20°, have been plotted. Data are *globally* fitted using the spring model (Eq. 3) (black lines). The global parameters obtained from the fit are: $D_T = 0.28 \pm 0.02$ μm^2/s, $\langle r_{int}^2 \rangle = 2.3 \pm 0.4 \times 10^{-3}$ μm^2 and $\xi = 0.16 \pm 0.01$ ms^{-1}.

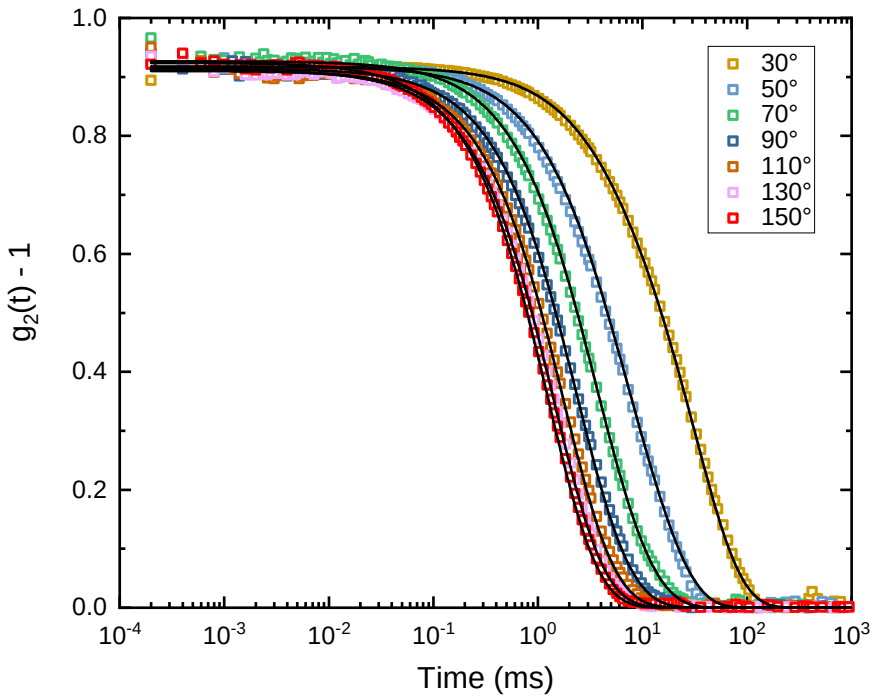

FIG. S7. **Intensity correlation function $g_2(q,t)$ of star particle suspensions at $\mathbf{OD_{520} = 0.17}$ measured by dynamic light scattering** for various scattering angles θ (symbols) from 30° to 150° in steps of 10°. For clarity, only half of the angles, *i.e.* every 20°, have been plotted. Data are *globally* fitted using the spring model (Eq. 3) (black lines). The global parameters obtained from the fit are: $D_T = 0.33 \pm 0.02$ μm^2/s, $\langle r_{int}^2 \rangle = 1.7 \pm 0.4 \times 10^{-3}$ μm^2 and $\xi = 0.18 \pm 0.01$ ms^{-1}.